

# Cyclic voltammetry electrodynamic deposition of $\text{Co}_{9-x}\text{Mn}_x\text{S}_8$ nanosheet array for electrocatalytic hydrogen evolution

Di Gao,<sup>a</sup> Peng Xiao<sup>\*b</sup> and Yunhuai Zhang<sup>\*a</sup>

<sup>a</sup>*College of Chemistry and Chemical Engineering, Chongqing University, Chongqing  
401331, China*

<sup>b</sup>*Chongqing Key Laboratory of Soft Condensed Matter Physics and Smart Materials,  
College of Physics, Chongqing University, Chongqing 401331, China*

† Electronic supplementary information (ESI) available.

## Corresponding Authors

To whom correspondence should be addressed:

(\*Y. H. Zhang) Tel.: +86 2365678362. E-mail: zyh2031@cqu.edu.cn

(\*P. Xiao) Tel.: +86 2365678362. E-mail: xiaopeng@cqu.edu.cn

## Notes

The authors declare no competing financial interest.

## 1. EXPERIMENTAL SECTION

### 1.1. Chemicals and materials

All chemicals were used as received from the Sigma-Aldrich without further purification, including cobalt nitrate hexahydrate ( $\text{Co}(\text{NO}_3)_2 \cdot 6\text{H}_2\text{O}$ , 99.5%), manganese chloride tetrahydrate ( $\text{MnCl}_2 \cdot 4\text{H}_2\text{O}$ , 99.8%), potassium chloride (KCl, 99%), thioacetamide ( $\text{CH}_3\text{CSNH}_2$ , 99%). Titanium (Ti) wafer (500  $\mu\text{m}$  thick, 99% pure) was purchased from Goodfellow Cambridge, Ltd. Ti working electrode were cut from wafers at  $1 \times 2 \text{ cm}^2$  size. Individual solutions were freshly prepared in deionized (DI) water (18.25  $\text{M}\Omega \cdot \text{cm}$ , purified through a Millipore system) for each deposition session.

The  $\text{Co}_{9-x}\text{Mn}_x\text{S}_8$  catalyst with different morphology and composition were electrochemically co-deposited onto the Ti wafer in a standard three-electrode glass setup using an electrochemical workstation (CHI660D). A graphite sheet, Ag/AgCl (3 M KCl), and a piece of Ti wafer with a geometric area of  $1 \text{ cm} \times 1 \text{ cm}$  acted as auxiliary, reference, and working electrodes, respectively. Prior to each deposition, the Ti foil was pretreated ultrasonically with 18% HCl aqueous solution for 15 min to remove the external oxide layer, followed by subsequent sonication in absolute ethanol. Afterwards, the working electrode was rinsed in DI water and dried in a stream of  $\text{N}_2$ .

### 1.2. Electrochemical co-deposition of $\text{Co}_{9-x}\text{Mn}_x\text{S}_8$ nanosheet array

$\text{Co}_{9-x}\text{Mn}_x\text{S}_8$  nanosheet arrays were deposited on a Ti substrate served as the current collector. The Ti foil dipped into electrolyte was fixed to be  $1 \times 1 \text{ cm}^2$ . The distance

between the counter electrode and the Ti sheet was kept to be  $\sim 2.5$  cm. A deposition bath containing 0.0503 M  $\text{CH}_3\text{CSNH}_2$  and different concentrations of  $\text{Co}(\text{NO}_3)_2$  and  $\text{MnCl}_2$  was freshly prepared for the synthesis of  $\text{Co}_{0.9-x}\text{Mn}_x\text{S}_8$  nanosheet. Increasing ion concentration could shorten the deposition time and raise the fabrication efficiency.  $\text{CH}_3\text{CSNH}_2$  (0.005 M) was used as the source sulfur, combined with ammonia for regulating the pH and stabilizing the metal ions. Neutral or near neutral deposition bath of simple composition and good stability is favored. We adjusted the pH value of all solutions to  $\sim 6.5$ . KCl was added in excess to facilitate the cathodic deposition via manipulating the reaction kinetics by affecting the redox potentials of metal precursor ions. The electrodynamic deposition was accomplished by applying cyclic voltammetry technique in a voltage range of -1.2 to 0.2 V vs. Ag/AgCl at a scan rate of  $2 \text{ mV s}^{-1}$  for 3 cycles. To avoid contamination, the “as-deposited” films were quickly removed from the bath after deposition and submerged into  $18.25 \text{ M}\Omega\cdot\text{cm}$  water bath to rinse off the excess solution for 1.5 h. Then the samples underwent vacuum drying at  $60 \text{ }^\circ\text{C}$  for 10 hours. We use a microbalance to determine the mass loading by the mass difference before and after the deposition.

### **1.3. Material characterization**

The morphology and microstructure of the samples were characterized by field emission scanning electron microscopy (FE-SEM, JEOL, JSM-7800F) and high resolution transmission electron microscope (HRTEM, FEI Tecnai G2F20, America, 200 kV). Power X-ray diffraction (PXRD) patterns of as-deposited catalysts were carried out with a Bruker D8 Advance X-ray diffractometer system operating at 40

kV equipped with a Co K $\alpha$  radiation ( $\lambda = 1.7902 \text{ \AA}$ ). Compositional information and valence states were determined by X-ray photoelectron spectroscopy (XPS, ESCALAB 250) with an Mg K $\alpha$  excitation source. All materials were charge neutralized with an in-lens electron source and grounded to the platform using a conductive clip to minimize charging. The resulting spectra was investigated with a Shirley background, calibrated using the substrate C 1s peaks (284.6 eV), and peak fit employing XPS Peak 41 software.

#### 1.4. Electrocatalytic measurements

Electrocatalytic performance of the electrodes were all achieved by a computer-controlled CHI660D electrochemical workstation in a typical three-electrode (full-cell) configuration. The Co<sub>9-x</sub>Mn<sub>x</sub>S<sub>8</sub> nanosheet arrays deposited on Ti sheet served as the working electrode. A graphite sheet and a calibrated Ag/AgCl electrode (CH Instruments, sat. KCl) with salt bridge kit were used as the counter and reference electrodes, respectively. All the potentials in the LSV graphs were presented with reference to the reversible hydrogen electrode (vs. RHE) through calibration by the Nernst relation below:<sup>1</sup>

$$E \text{ (vs. RHE)} = E \text{ (vs. Ag/AgCl)} + E_{\text{Ag/AgCl}}^{\text{reference}} + 0.0591\text{pH}$$

where  $E_{\text{Ag/AgCl}}^{\text{reference}} = 0.197$  vs. RHE at 298 K. 0.5 M H<sub>2</sub>SO<sub>4</sub> or 1 M KOH solution were employed as electrolyte under continuous purging with H<sub>2</sub> for all electrochemical tests, which have constant pH of 0 or 13. Linear sweep voltammetry (LSV) tests were performed at a scan rate of 5 mV s<sup>-1</sup>. *IR* (solution internal resistance) compensation was applied in all the LSV experiments. The polarization curves were plotted as overpotential ( $\eta$ ) versus log current ( $\log j$ ) to obtain Tafel plots for assessing

the HER kinetics. Current density was normalized to the geometrical area of the working electrode. Cyclic Voltammetry (CV) and Chronopotentiometric tests (V-t) were carried out without  $iR$  compensation. The electrochemically active surface (ECSA) of the catalysts was calculated using the electrochemical double-layer capacitance ( $C_{DL}$ ) of the catalytic surface according to equation  $ECSA = C_{DL}/C_s$ ,<sup>2,3</sup> where  $C_s$  is the specific capacitance. As the double-layer charging current ( $i_c$ ) in non-Faradic potential region is proportional to the scan rate ( $i_c = \nu C_{DL}$ , where  $\nu$  is the scan rate),  $C_{DL}$  values were derived via cyclic voltammetry (CV) tests at different scan rates. From a plot of the capacitive current density ( $i_c$ ) against the scan rate ( $\nu$ ), the resulting linear slope yields the  $C_{DL}$ .<sup>4</sup>

## 2. SUPPORTING TABLES AND FIGURES

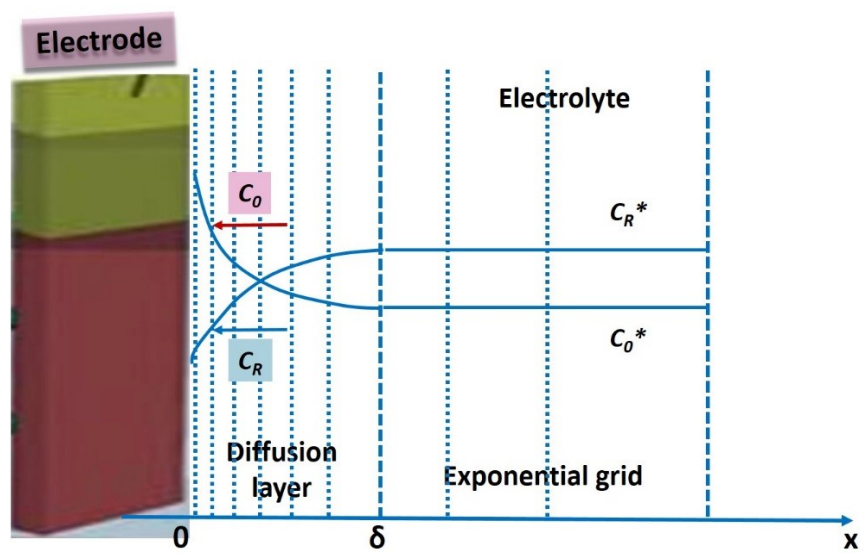


**Fig. S1** Concentration profile and exponential grid.

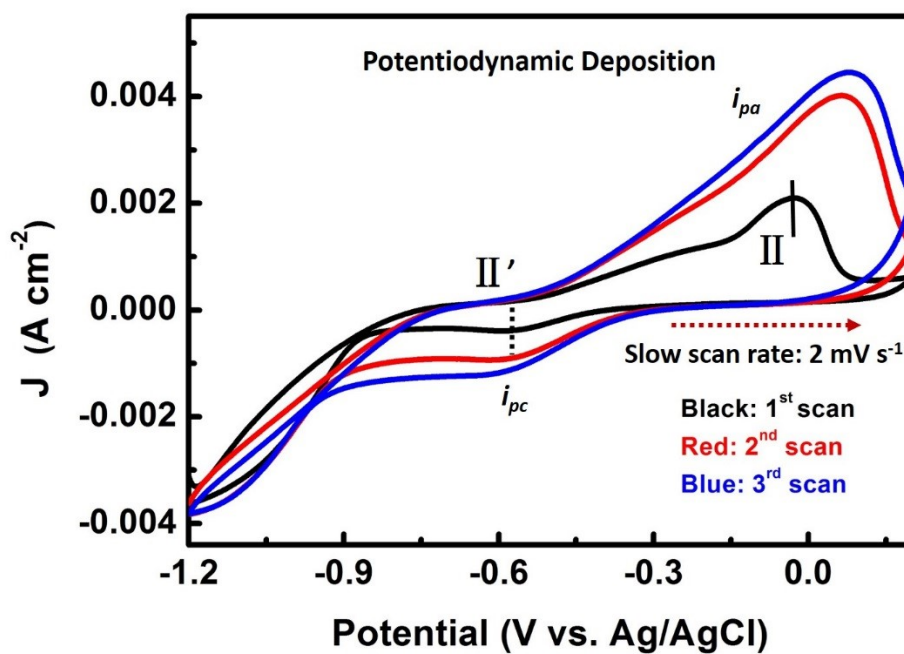


**Fig. S2** Cyclic voltammograms curves recorded at a low scan rate of  $2 \text{ mV s}^{-1}$  in the complex electrolyte containing  $0.015 \text{ M Co(NO}_3)_2$  and  $0.0503 \text{ M CH}_3\text{CSNH}_2$ .

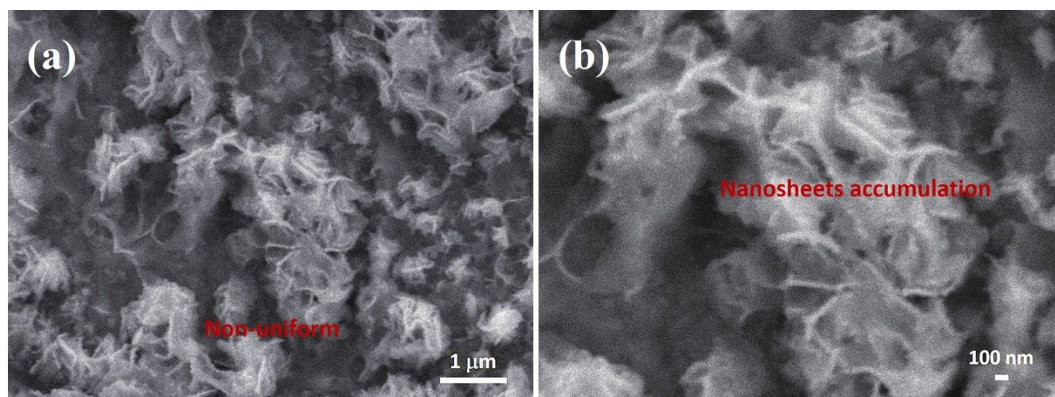


**Fig. S3** Representative SEM images of  $\text{Co}_{9-x}\text{Mn}_x\text{S}_8$  ( $x=4.5$ ) nanosheets at (a) low- and (b) high- magnifications fabricated by cyclic voltammogram electrodynamic deposition at a high scan rate of  $8 \text{ mV s}^{-1}$ .

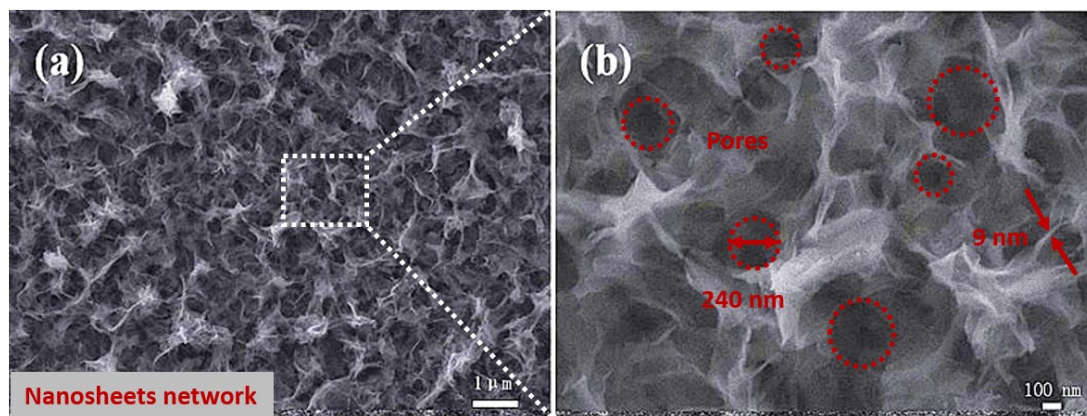


**Fig. S4** Typical SEM micrographs of  $\text{Co}_9\text{S}_8$  nanosheets network: (a) overall view at low magnification, (b) enlarged view of the nanosheets structure at high magnification.

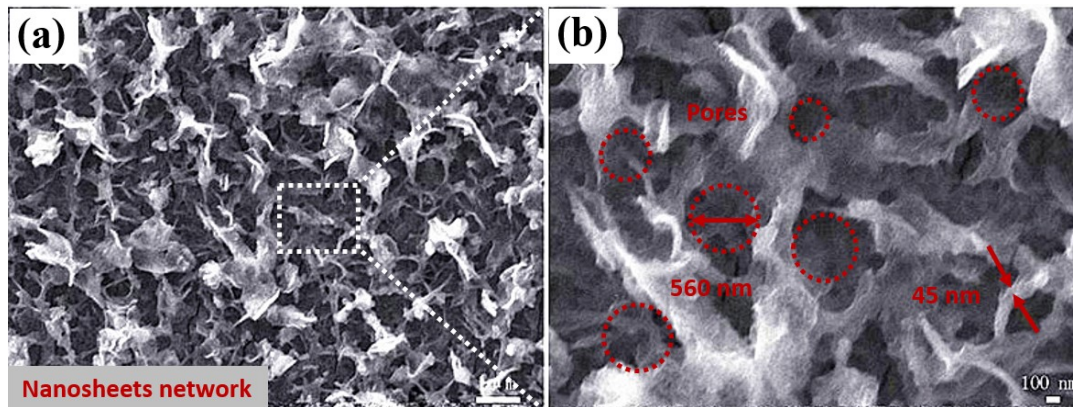


**Fig. S5** Typical SEM micrographs of  $\text{Co}_{9-x}\text{Mn}_x\text{S}_8$  ( $x = 6$ ) nanosheets array: (a) overall view at low magnification, (b) enlarged view of the nanosheets structure at high magnification.

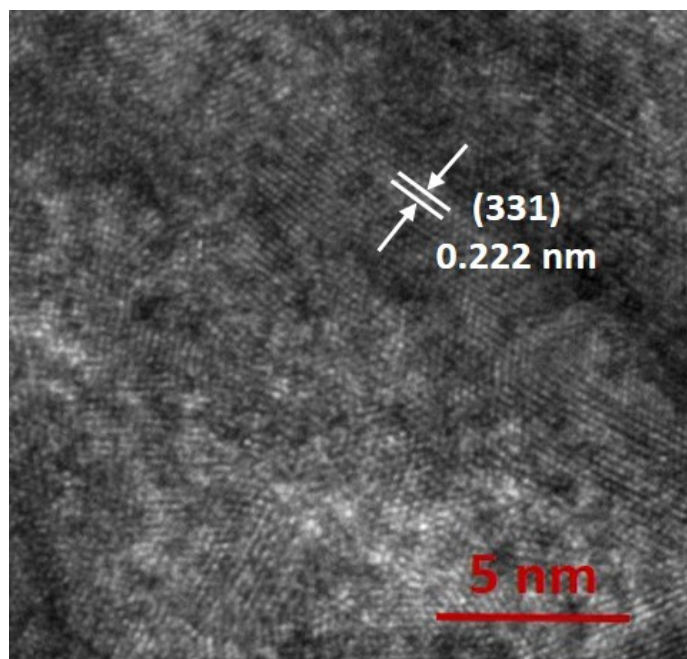


**Fig. S6** Magnified image of pristine Co<sub>9</sub>S<sub>8</sub> thin nanosheets, showing the crystalline structure.

**Table S1** Correspondence between atomic ratio of Co/Mn in the baths and films for the catalysts.

Catalyst	Baths		Films	
	x	Atomic ratio (Co/Mn)	x	ICP-MS measured atomic ratio (Co/Mn)
Co <sub>9-x</sub> Mn <sub>x</sub> S <sub>8</sub>	3	2:1	0.6	14.0:1
Co <sub>9-x</sub> Mn <sub>x</sub> S <sub>8</sub>	4.5	1:1	1.2	6.5:1
Co <sub>9-x</sub> Mn <sub>x</sub> S <sub>8</sub>	6	1:2	2.0	3.5:1

**Note 1** Correspondence between the atomic ratio of Co and Mn in the baths and films (determined by ICP-MS) is shown in Table S1. As displayed in Table S1, with the incremental Mn concentration in the baths, Mn proportion in the samples did not increase linearly. The composition of deposited film doesn't approach the electrolyte composition. A slight reduction in film composition was observed with higher Mn content in baths. At specific electrodeposition bath conditions, above phenomenon is probably largely due to the faster electrodeposition rate of Co than Mn.

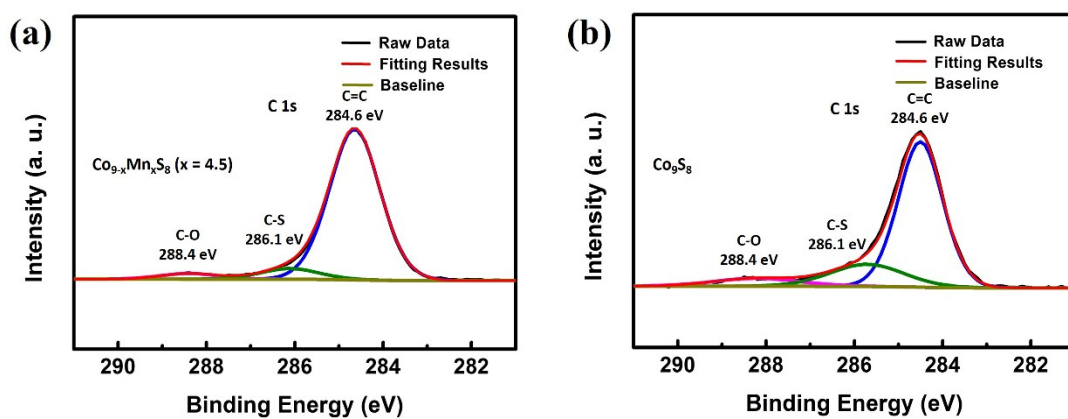


**Fig. S7** XPS spectrum for C 1s region of (a)  $\text{Co}_{9-x}\text{Mn}_x\text{S}_8$  ( $x = 4.5$ ), and (b) pristine  $\text{Co}_9\text{S}_8$ , respectively.

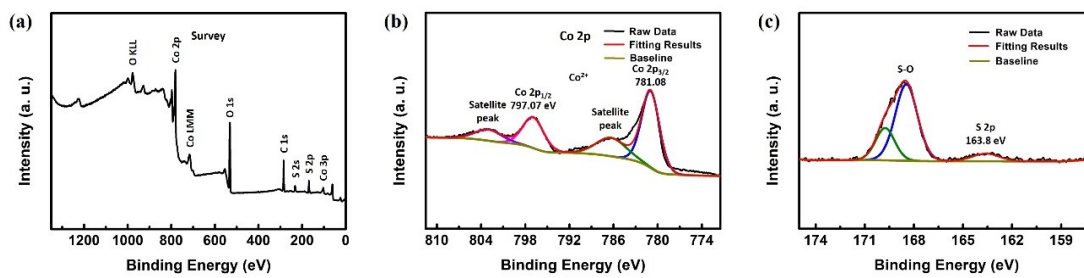


**Fig. S8** XPS spectrum of pristine  $\text{Co}_9\text{S}_8$  for (a) survey, (b) Co 2p, and (c) S2p regions, respectively. Black lines are the measured XPS spectra, and the red lines are the fitting results of the sum of individual components. Color codes are used for indication of different spin-orbit components.

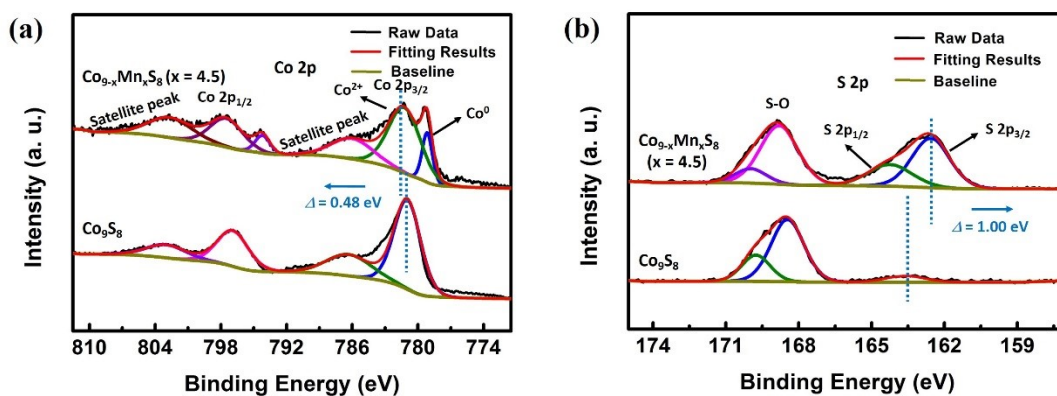


**Fig. S9** High-resolution XPS spectra for (a) Co 2p, (b) S 2p regions of  $\text{Co}_9\text{S}_8$  (bottom) and  $\text{Co}_{9-x}\text{Mn}_x\text{S}_8$  ( $x = 4.5$ ) (top), respectively.

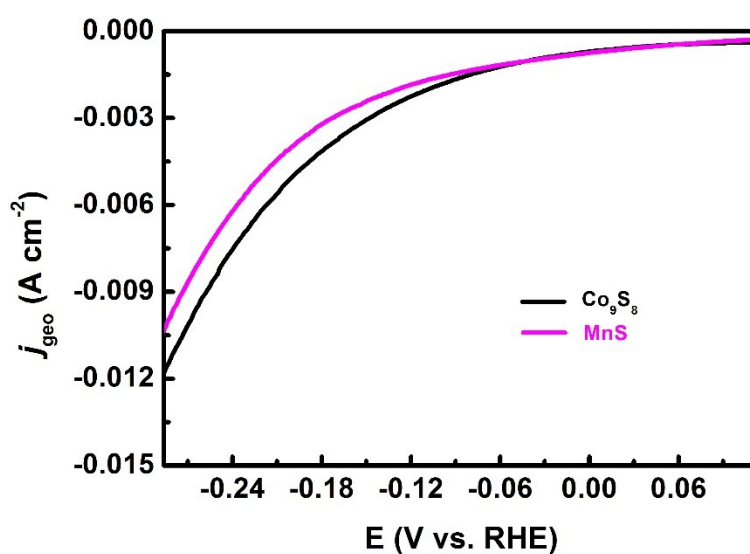


**Fig. S10** Electrocatalytic HER performance of Co<sub>9</sub>S<sub>8</sub> and MnS electrocatalysts with *IR*-corrected LSVs tested in 0.5 M H<sub>2</sub>SO<sub>4</sub> medium.

**Note 2** As shown in Fig. S10, manganese sulfide (MnS) has comparable HER activity to that of Co<sub>9</sub>S<sub>8</sub> in acidic medium, approaching -10 mA cm<sup>-2</sup> at a  $\eta$  value of 287.8 mV. However, in alkaline electrolyte MnS displays negligible HER catalytic effect (Fig. S11).

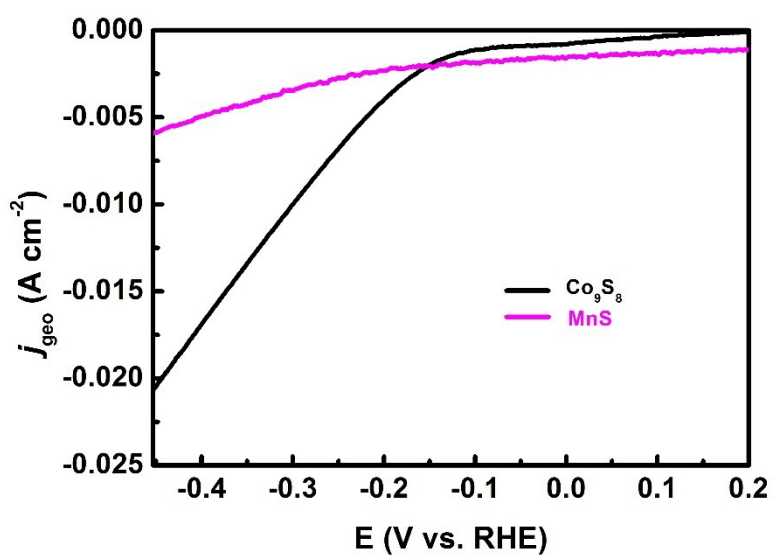


**Fig. S11** Electrocatalytic HER performance of  $\text{Co}_9\text{S}_8$  and MnS electrocatalysts with  $iR$ -corrected LSVs tested in 1M KOH medium.

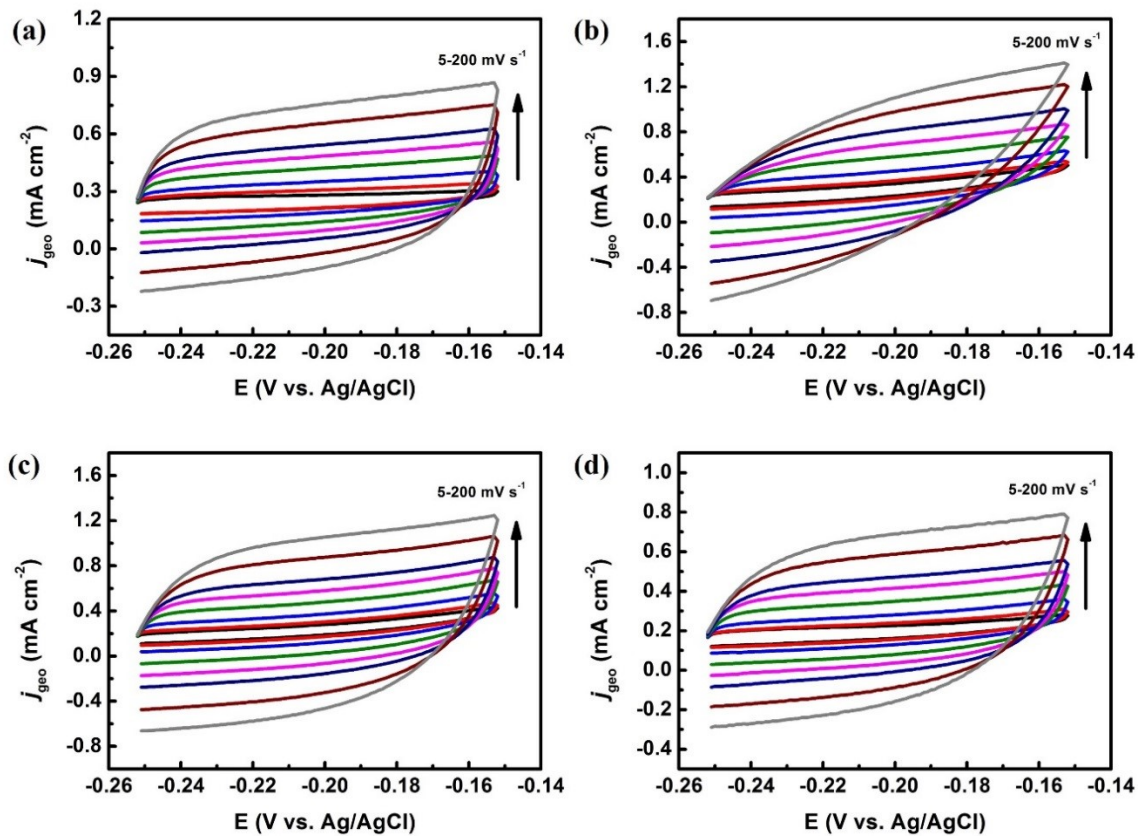


**Fig. 12** CVs of (a) pristine  $\text{Co}_9\text{S}_8$  and  $\text{Co}_{9-x}\text{Mn}_x\text{S}_8$  films with (b)  $x = 3$ , (c)  $x = 4.5$ , (d)  $x = 6$  measured in a non-Faradaic region of the voltammograms at various scan rates from 5 to 200  $\text{mV s}^{-1}$  in 1 M KOH solution.

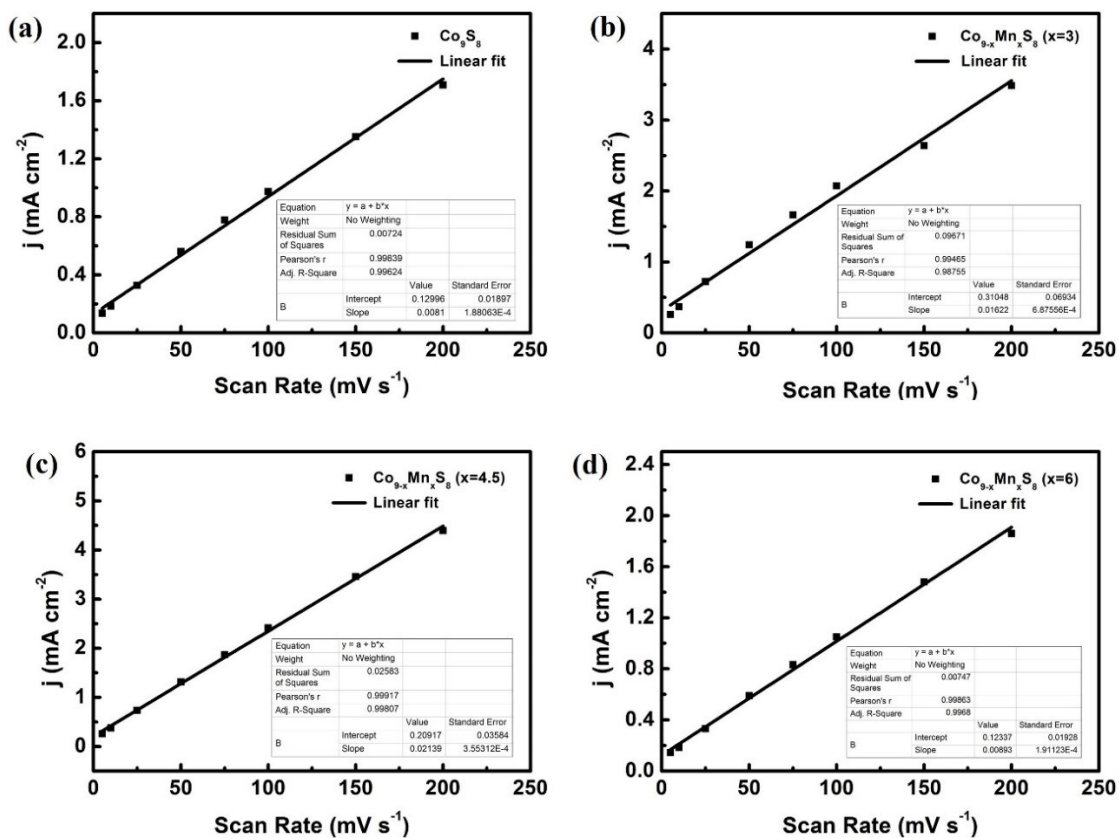


**Fig. 13** Corresponding capacitive current density at a specific potential vs. Ag/AgCl as a function of scan rates for as-deposited electrocatalysts.

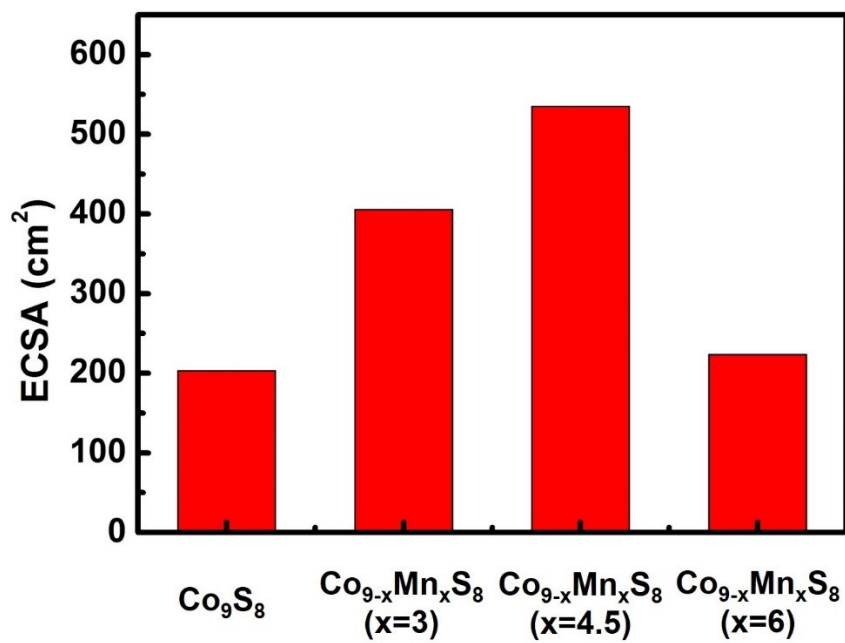


**Fig. S14** Histogram of the values of the electrochemical active surface area (ECSA)

of Co<sub>9</sub>S<sub>8</sub> and Co<sub>9-x</sub>Mn<sub>x</sub>S<sub>8</sub> samples.

**Table S2** Summary of the  $C_{dl}$ , ECSA, roughness, and specific surface area.

Catalysts	$C_{dl}$ (mF cm <sup>-2</sup> )	ECSA (cm <sup>2</sup> )	Roughness	Specific surface area (cm <sup>2</sup> /mg)
Co <sub>9</sub> S <sub>8</sub>	8.12	203.1	203.1	406.2
Co <sub>9-x</sub> Mn <sub>x</sub> S <sub>8</sub> (x=3)	16.22	405.5	405.5	811.0
Co <sub>9-x</sub> Mn <sub>x</sub> S <sub>8</sub> (x=4.5)	21.39	534.7	534.7	1069.4
Co <sub>9-x</sub> Mn <sub>x</sub> S <sub>8</sub> (x=6)	8.93	223.2	223.2	446.4

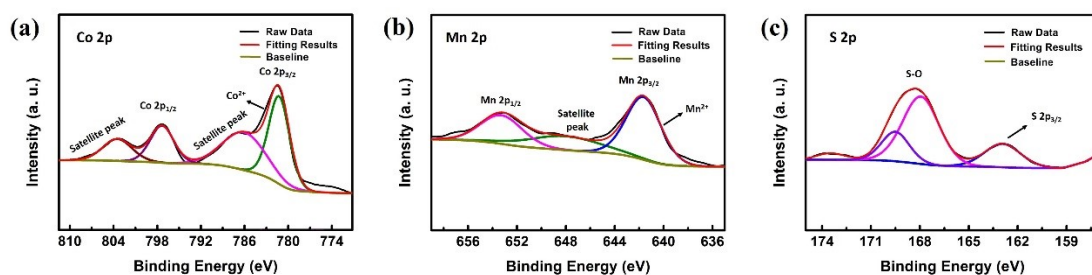


**Fig. S15** XPS spectrum of  $\text{Co}_{9-x}\text{Mn}_x\text{S}_8$  ( $x = 4.5$ ) after durability test for (a) Co 2p, (b) Mn 2p, and (c) S 2p regions, respectively. Black lines are the measured XPS spectra, and the red lines are the fitting results of the sum of individual components. Color codes are used for indication of different spin-orbit components.

**Note 3** We have supplemented the XPS data of the  $\text{Co}_{9-x}\text{Mn}_x\text{S}_8$  ( $x = 4.5$ ) after durability test. The surface morphology of the  $\text{Co}_{9-x}\text{Mn}_x\text{S}_8$  ( $x = 4.5$ ) electrode remains intact after the V-t test. The rippled nanoarray is almost completely preserved, and no noticeable dissolution or detachment occurs (Fig. 5d and e). However, as shown in Fig. S15, the peak of  $\text{Co}^0$  disappears after HER, which may be attributed to the partial change of  $\text{Co}^0$  to high valence states. This factor might be the reason why the HER activity changes to a certain extent.

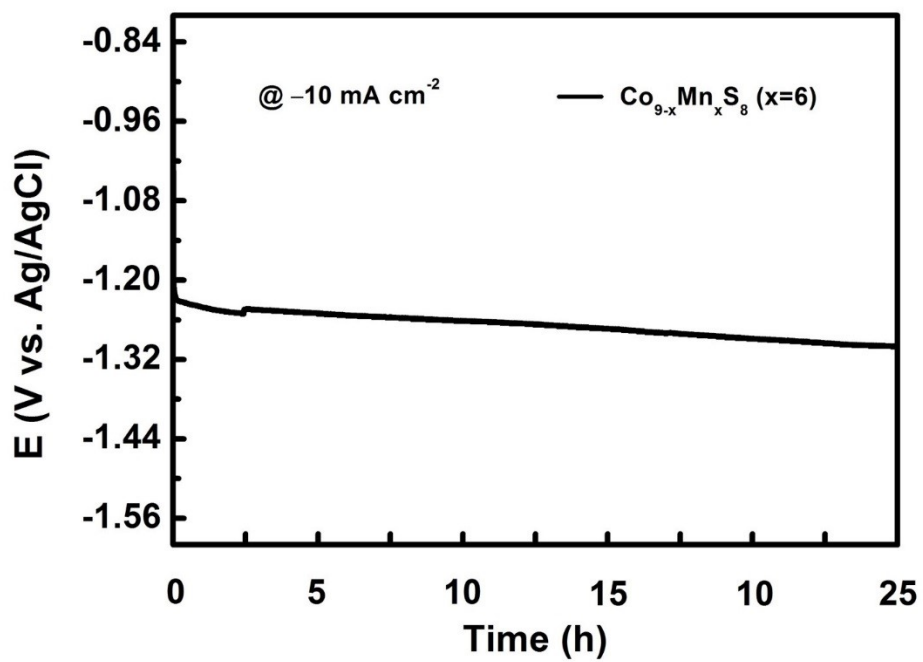


**Fig. S16** Chronopotentiometric test of  $\text{Co}_{9-x}\text{Mn}_x\text{S}_8$  ( $x = 6$ ) catalyst at  $-10 \text{ mA cm}^{-2}$  up to 25 h.

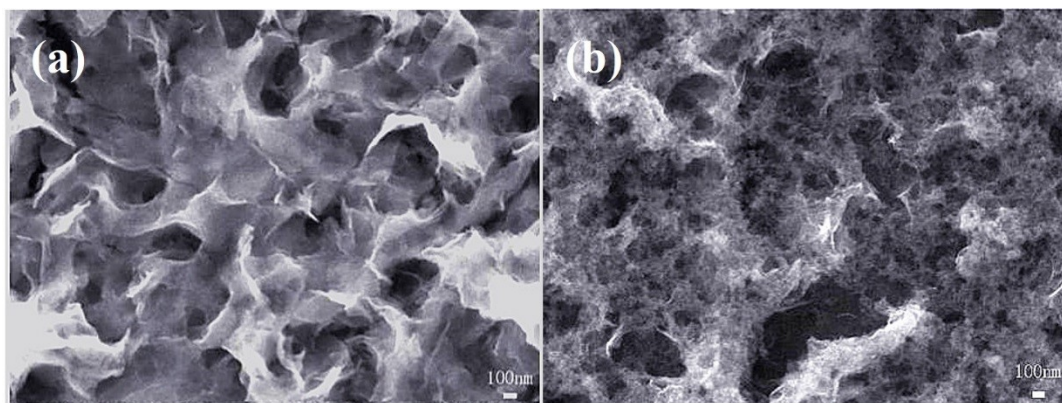


**Fig. S17** Comparison of SEM micrographs of  $\text{Co}_{9-x}\text{Mn}_x\text{S}_8$  ( $x = 6$ ) (a) before, (b) after the chronopotentiometric test.

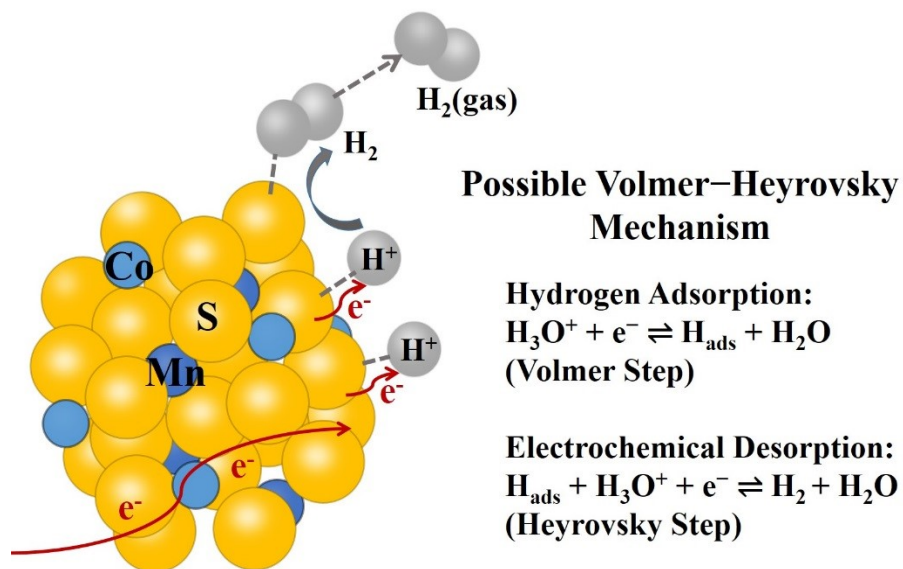


**Fig. S18** Schematic reaction pathway of  $\text{H}_2$  evolution on sulfur atoms of  $\text{Co}_{9-x}\text{Mn}_x\text{S}_8$  ( $x=4.5$ ) edges in acidic medium.

**Table S3** Tafel slope,  $\eta_{10}$ , and  $j_0$  comparison of the state-of-the-art materials based on transition metal sulfides.

Catalysts	$\eta$ (mV) @- 10 mA cm <sup>-2</sup>	Tafel slope (mV dec <sup>-1</sup> )	$J_0$ (mA cm <sup>-2</sup> )	Electrolyte
Co/MoS <sub>2</sub>	156	58	N.A.	0.5 M H <sub>2</sub> SO <sub>4</sub>
Te doped WS <sub>2</sub>	213	94	N.A.	0.5 M H <sub>2</sub> SO <sub>4</sub>
MoS <sub>2</sub> 10K	248	61	N.A.	0.5 M H <sub>2</sub> SO <sub>4</sub>
Zn-Co <sub>9</sub> S <sub>8</sub> @CF-(1-1)	273	85.2	N.A.	0.5 M H <sub>2</sub> SO <sub>4</sub>
N-NiCo <sub>2</sub> S <sub>4</sub>	41	37	N.A.	1 M KOH
Se-(NiCo)S <sub>x</sub> /(OH) <sub>x</sub>	103	83	N.A.	1 M KOH
Co <sub>0.9</sub> S <sub>0.58</sub> P <sub>0.42</sub>	141	72	N.A.	0.1 M KOH
Ni-Co-MoS <sub>2</sub>	155	51	N.A.	1 M KOH
CoMoNiS-NF	113	58	N.A.	1 M KOH
MoS <sub>2</sub> /Ni <sub>3</sub> S <sub>2</sub>	110	83.1	N.A.	1 M KOH
TiO <sub>2</sub> @Co <sub>9</sub> S <sub>8</sub>	139	65	N.A.	1 M KOH
Co <sub>9</sub> S <sub>8</sub>	222	85	N.A.	1 M KOH
CoS/MoS <sub>2</sub>	180	72	N.A.	1 M KOH
Fe-NiS <sub>2</sub> /MoS <sub>2</sub>	120	119.9	N.A.	1 M KOH
MoO <sub>2</sub> /MoS <sub>2</sub> /C	91	49	N.A.	1 M KOH

### 3 REFERENCES

- 1 D. Gao, J. Guo, X. Cui, L. Yang, Y. Yang, H. He, P. Xiao and Y. Zhang, *ACS Appl. Mater. Interfaces*, 2017, **9**, 22420-22431.
- 2 Q. Ma, C. Hu, K. Liu, S. F. Hung, D. Ou, H. M. Chen, G. Fu and N. Zheng, *Nano Energy*, 2017, **41**, 148-153.
- 3 Q. L. L. Zhong, C. Du, Y. Luo, Y. Zheng, S. Li and Q. Yan, *Nano Energy*, 2018, **47**, 257-265.
- 4 R. B. Wexler, J. M. P. Martirez and A. M. Rappe, *J. Am. Chem. Soc.*, 2018, **140**, 4678-4683.
- 5 J. Benson, M. Li, S. Wang, P. Wang and P. Papakonstantinou, *ACS Appl. Mater. Interfaces*, 2015, **7**, 14113–14122.
- 6 E. Navarro-Flores, Z. Chong and S. Omanovic, *J. Mol. Catal. A: Chem.*, 2005, **226**, 179–197.
- 7 Y. Yang, M. Zhou, W. Guo, X. Cui, Y. Li, F. Liu, P. Xiao and Y. Zhang, *Electrochim. Acta*, 2015, **174**, 246–253.
- 8 J. Li, Y. Wang, C. Liu, S. Li, Y. Wang, L. Dong, Z. Dai, Y. Li and Y. Lan, *Nat. Commun.*, 2016, **12**, 1-8.
- 9 X. Cui, W. Guo, M. Zhou, Y. Yang, Y. Li, P. Xiao, Y. Zhang and X. Zhang, *ACS Appl. Mater. Interfaces*, 2014, **12**, 493–503.
- 10 P. Chen, K. Xu, S. Tao, T. Zhou, Y. Tong, H. Ding, L. Zhang and W. Chu, *Adv. Mater.*, 2016, **10**, 1–6.